NOTES AND CORRESPONDENCE

Characteristics of Cloud Radiation Forcing over East China

WEI-CHYUNG WANG AND WEI GONG

Atmospheric Sciences Research Center, The University at Albany, State University of New York, Albany, New York

WEN-SHUNG KAU

Department of Atmospheric Sciences, National Taiwan University, Taipei, Taiwan

CHENG-TA CHEN

Department of Atmospheric Sciences, National Taiwan Normal University, Taipei, Taiwan

HUANG-HSIUNG HSU

Department of Atmospheric Sciences, National Taiwan University, Taipei, Taiwan

CHIA-HSIU TU

Institute of Information Science, Academia Sinica, Taipei, Taiwan

4 September 2002 and 21 January 2003

ABSTRACT

Observations indicate that the East Asian summer monsoon (EASM) exhibits distinctive characteristics of large cloud amounts with associated heavy and persistent rainfall, although short breaks for clear sky usually occur. Consequently, the effects of cloud–radiation interactions can play an important role in the general circulation of the atmosphere and, thus, the evolution of the EASM. In this note, as a first step toward studying the topic, the 5-yr (January 1985–December 1989) Earth Radiation Budget Experiment (ERBE) dataset is used to show the spatial and temporal patterns of both shortwave (SW) and longwave (LW) cloud radiative forcing (CRF) at the top of the atmosphere over east China, and to compare the observed features with Atmospheric Model Intercomparison Project-II (AMIP-II) simulations with the University at Albany, State University of New York (SUNYA) Community Climate Model 3 (CCM3) and the ECHAM4 general circulation models.

The observations indicate that the net CRF provides a cooling effect to the atmosphere–surface climate system, dominated by the SW CRF cooling (albedo effect) with partial compensation from the LW CRF warming (greenhouse effect). The SW CRF shows a strong seasonal cycle, and its peak magnitude is particularly large, $\sim$110 W m^{-2}, for south China and the Yangtze–Huai River valley (YHRV) during May and June, while the LW CRF is about 50 W m^{-2} for the same months with a weak dependence on the latitudes and seasons. These characteristics are in sharp contrast to the Northern Hemispheric zonal means of the same latitude bands and seasons, thus implying a unique role for cloud–radiation interaction in east China. Both model simulations show similar observed characteristics, although biases exist. For example, in May, the ECHAM4 underestimates the SW CRF while the SUNYA CCM3 simulates a significantly larger value, both attributed to the respective biases in the simulated total cloud cover. Model-to-observation comparisons of the association between total cloud cover and SW CRF, and between high cloud cover and LW CRF, are also presented and their differences are discussed. Finally, the SUNYA CCM3 biases in the CRF and its relevance to the model cloud biases are discussed in the context of model cold and dry biases in climate simulations.

1. Introduction

Observations indicate that the East Asian summer monsoon (EASM) shows distinctive characteristics of persistent and heavy rainfall (Ding 1994; Wang et al. 2000), which are intimately related to clouds. Although the direct effects of clouds on the shortwave (SW) and longwave (LW) radiation are fairly well understood, the role that clouds play in the evolution of the EASM has not been studied, in particular with regard to the aspects of heating and cooling attributed to clouds, and the comparison with heating caused by convection and large-scale condensa-

Corresponding author address: Dr. Wei-Chyung Wang, Atmospheric Sciences Research Center, The University at Albany, State University of New York, CESTM Bldg., 251 Fuller Rd., Albany, NY 12203.
E-mail: wang@climate.cestm.albany.edu

tion. Here, as a first step, we use observations to illustrate the spatial and temporal patterns of cloud radiative forcing (CRF), which is related to perturbations of the clear-sky radiation flux due to the presence of clouds (Potter et al. 1993 and references therein). Two terms, the SW CRF and LW CRF, are usually derived at either the top of the atmosphere (TOA) or at the surface.

There have been many studies of CRF using both observations and model simulations (e.g., Randall et al. 1989; Kiehl and Ramanathan 1990; Zhang et al. 1996; Cess et al. 2001). However, studies over East Asia, in particular for east China during the EASM, are lacking. In the present study, we focus on the TOA CRF simply because of the availability of satellite data from the Earth Radiation Budget Experiment (ERBE; Barkstrom 1984). Since the SW CRF refers, to a large extent, to the reflected solar radiation, its variation is believed to be closely related to the total cloud cover. On the other hand, the high clouds tend to more efficiently trap the outgoing LW radiation and therefore there exists a close link between the LW CRF and high cloud cover (see Weare 1995). Ockert-Bell and Hartmann (1992) used both International Satellite Cloud Climatology Project (ISCCP; Rossow and Schiffer 1991) and ERBE data to examine these aspects and found that the association is sensitive to cloud type.

The TOA CRF is a quantity that covers many aspects of cloud features effecting the SW and LW radiation, including the vertical structure of cloud distribution, the degree of cloud overlap, and cloud optical properties. Therefore, it is a ''macroscopic'' parameter, which offers an alternative approach (versus the ''microscopic'' approach, which includes cloud cover and cloud microphysical properties) for conducting model-to-observation comparisons. In this regard, we have also used the spatial and temporal patterns derived from observations to evaluate the Atmospheric Model Intercomparison Project-II (AMIP-II) simulations (see Gates et al. 1999), specifically the University at Albany, State University of New York (SUNYA), Community Climate Model 3 (SUNYA CCM3; Wong and Wang 2000) and ECHAM4. Below, the data used for the CRF and cloud analysis are given in section 2, while analyses of the spatial and temporal patterns and their associations with clouds as well as model biases are presented in section 3. Section 4 discusses further work.

2. Climate data

Monthly mean values of cloud cover and CRF from both observations and global climate model simulations during the period January 1985–December 1989 are used to study their individual characteristics and their association over east China. The observational data consist of the SW and LW CRF data from ERBE (information available online at http://iridl.ldeo.columbia.edu/SOURCES/.NASA/.ERBE/.ERBS/.cloud-forcing/), and the total and high (50–440 hPa) cloud cover data from ISCCP-C2 (information online at http://ingrid.ldeo.columbia.edu/SOURCES/GEDEX/.isccp_c2.cdf). As a consistency check, the surface observations of total cloud cover in China (online at http://cdiac.ornl.gov/ftp/ndp039/) are also used; 41 of the 65 stations are located within the study domain of east China. For model simulations, we used SUNYA CCM3 and ECHAM4 AMIP-II simulated cloudiness and CRF data; both models used prescribed, observed monthly mean sea surface temperatures and sea ice. Note that to further analyze the effect of the cloud vertical distribution on CRF, we have extracted the high (50–400 hPa) and total cloud cover from the model simulations. There is a small difference in the range of the model high clouds versus ISCCP's range. In the study, the 5-yr-mean values for both observations and model simulations are used to illustrate the spatial and temporal patterns over east China, although for the association between the total cloud cover and SW CRF, and between high cloud cover and LW CRF, we used the monthly data of individual years directly.

However, it is important to recognize that there exists uncertainty in the observational datasets, and in direct comparisons between model simulations and observations. For ERBE, the uncertainties are related to the instrument precision, data sampling, and data retrieval and conversion technique; for example, for data sampling in some regions where overcast sky was persistent, monthly averaged clear sky flux is usually used to calculate the CRF. Nevertheless, as pointed out by Harrison et al. (1990), these uncertainties are usually less than a few percent. On the other hand, although the monthly mean cloud cover from ISCCP-C2 agrees well with ground-based observations (e.g., Fu et al. 1990; Minnis et al. 1993), which is also confirmed by our comparison over east China, discussed in section 3b, there exist uncertainties in the direct comparison of GCM-simulated cloud cover versus that from the observations. For example, the total cloud cover in the satellite observations is calculated from the number of cloud pixels compared to the total number of pixels, while the modeled total cloud cover is computed with cloud cover at each model level using certain overlapping assumptions (Liang and Wang 1997). As a result, a quantitative comparison of cloud cover between model simulations and observations remains a critical issue.

3. Analysis

The latitudinal–seasonal distribution of the net cloud radiative forcing averaged over 105°–122°E is shown in Fig. 1a for the observations and in Fig. 1b for SUNYA CCM3. Clearly, for the latitudes 20°–30°N, there exists a strong net cooling (>50 W m^{-2}) during the first 6 months of the year, and again in September–October due to the retreat of the rainbelt (Wang et al. 2000). During northern summer, the -25 W m^{-2} cooling contour extends farther into the high latitudes. For SUNYA

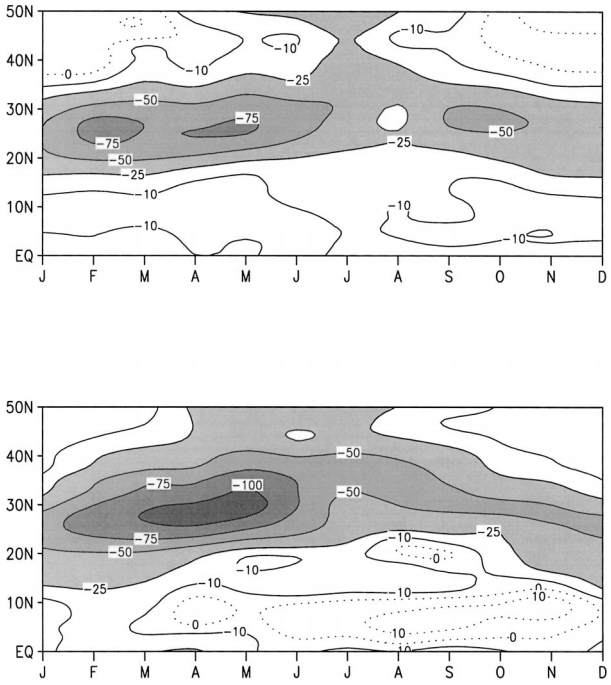

FIG. 1. The 1985–89 mean annual cycle of net (longwave and shortwave) cloud radiative forcing (W m^{-2}) averaged over 105°–122°E from (top) ERBE and (bottom) SUNYA CCM3 data.

CCM3 simulations, although the spatial and seasonal characteristics are similar, the model shows larger CRF values as well as stronger seasonal variation, in particular during March–May.

Because of the CRF contour structure shown in Fig. 1, the regional means of three regions—south China (23°–30°N, 105°–122°E), the Yangtze–Huai River valley [YHRV; (30°–34°N, 105°–122°E)], and north China (34°–43°N, 105°–122°E)—are used for all of the analyses described below. The three regions are also consistent with the precipitation characteristics studied in Samel et al. (1999) and Liang et al. (2001). In addition, the corresponding zonal values averaged over the Northern Hemisphere (NH) are also used to contrast the corresponding characteristics from east China.

a. Annual cycle of regional cloud radiative forcing

1) OBSERVATIONS

The 5-yr mean annual cycles of the net CRF for the three regions over east China are shown in Fig. 2a. As expected, throughout the year, the presence of clouds is responsible for significant cooling of the atmosphere–surface climate system in these regions, showing a decrease in magnitude going northward except in summer. For south China, the seasonal variation is quite substantial and it is particularly striking that the intensity of the cooling decreases from a maximum of ~70 W m^{-2} in May, to a minimum of ~25 W m^{-2} in August and then increases to ~50 W m^{-2} in September–October. A similar seasonal variation is observed in the YHRV, although the amplitude is slightly smaller. For north China, the peak cooling of ~35 W m^{-2} occurs in July, lagging 2 months behind south China and the YHRV. The NH zonal mean values corresponding to the three regions are shown in Fig. 2b. It is interesting to note that the zonal mean CRF shows an increase in magnitude going northward, which is opposite to those in east China. In addition, the difference in the intensity is also quite evident, suggesting the significant role clouds play in radiative forcing over east China throughout the year.

Next, we examine the separate SW and LW CRFs. The observed annual cycles of the SW and LW CRFs for the YHRV and north China, and their corresponding NH zonal means, are shown in Fig. 3a. (Note that south China exhibits similar features as the YHRV and its characteristics are not shown here.) As expected, the SW CRF cooling dominates, which is partially compensated (about 50%) by the warming due to the LW CRF. Three features are noted here. First, over the

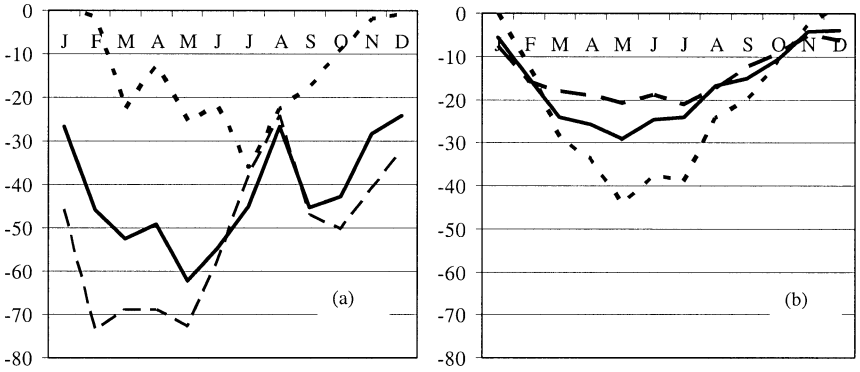

FIG. 2. The 1985–89 mean annual cycle of net (longwave and shortwave) cloud radiative forcing (W m^{-2}) for (a) south China (23°–30°N, 105°–123°E; dashed line), the YHRV (30°–34°N, 105°–123°E; solid line), and north China (34°–43°N, 105°–123°E; dotted line), and (b) the Northern Hemispheric zonal means over 23°–30°, 30°–34°, and 34°–43°N to show their contrast to south China, the YHRV, and north China, respectively.

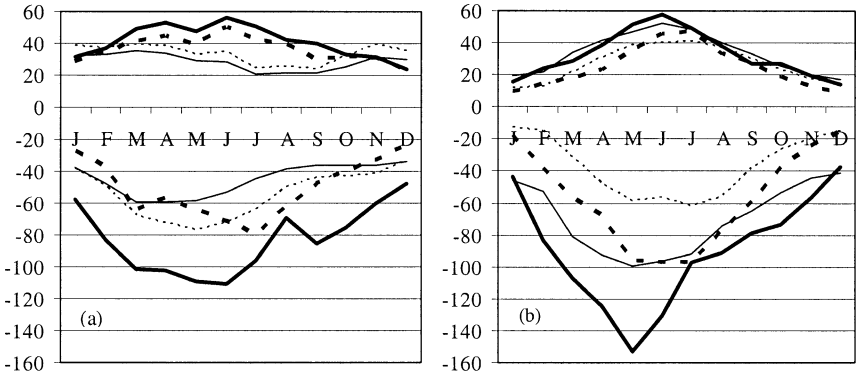

FIG. 3. Annual cycle of longwave (positive) and shortwave (negative) cloud radiative forcing (W m^{-2}) averaged over 1985–89. The lines are thick solid for the YHRV (30°–34°N, 105°–123°E) and thick dashed for north China (34°–43°N, 105°–123°E). (a) ERBE data. The thin solid and dashed lines correspond, respectively, to Northern Hemispheric zonal means of 30°–34° and 34°–43°N to show their contrast to the respective YHRV and north China regions. (b) AMIP models. The thick lines are for the SUNYA CCM3 and thin lines are for ECHAM4.

YHRV, the SW CRF increases from about 60 W m^{-2} in January to 100 W m^{-2} in March, and reaches a peak value 110 W m^{-2} in June. There is a sharp decrease to 70 W m^{-2} in August, then a slight recovery, and finally a decrease afterward. For north China, the SW CRF increases to 60 W m^{-2} in March and remains relatively constant until it peaks at of 80 W m^{-2} in July, lagging 1 month behind the maximum of the YHRV. These characteristics during the March–September period reflect the northward movement of the rainbelt from south China to the YHRV in spring and early summer, and from the YHRV to north China in late summer and early fall (Ding 1994; Wang et al. 2000). However, because of the monthly mean data used, the characteristics cannot possibly reflect the observed shorter time-scale rainfall fluctuations; for example, in mid-June the monsoon precipitation begins over the YHRV, which is known as the mei-yu, or plum rain. Compared to the SW CRF, the LW CRF annual cycle is much weaker, although the period for peak values (March–August) coincides with that of the SW CRF.

Second, the difference in the seasonal variation between north China and the YHRV is small in the LW CRF, but significant in the SW CRF. For example, during the period of May–June, when the maximum SW CRF (about 110 W m^{-2}) occurred in the YHRV, the difference between the two regions is about 50 W m^{-2} in SW CRF, but less than 10 W m^{-2} in LW CRF. Third, the SW and LW CRF for north China and the YHRV show different seasonal variations when compared with their respective Northern Hemispheric zonal mean values. The difference is particularly large in the YHRV; for example, for SW CRF, it is about 50 W m^{-2} in May and 60 W m^{-2} in June, and the differences in the respective LW CRFs are 20 and 30 W m^{-2}. For north China, the contrast in SW CRF between the regional mean and its corresponding NH zonal mean is much smaller (than in the YHRV); for example, the difference in June is about 18 W m^{-2}, about one-third of the value in the YHRV. This deviation of the regional mean from the NH zonal mean in the YHRV reflects its unique position within the large-scale heating/cooling distribution in the Northern Hemisphere.

2) SUNYA CCM3 AND ECHAM4 AMIP-II MODEL SIMULATIONS

The characteristics shown in Fig. 3a were also diagnosed using SUNYA CCM3 and ECHAM4 AMIP-II model simulations, and the results are shown in Fig. 3b. For the SW CRF, both models qualitatively capture the observed annual cycles of the YHRV and north China as well as the contrast between the YHRV and north China. Note that south China exhibits similar features as in the YHRV and its characteristics are not shown here.

However, model biases exist when compared with observations shown in Fig. 3a. The ECHAM4, which simulates well the SW CRF (within 15 W m^{-2}) of the YHRV observations during April–August, yields much smaller values (about 30–40 W m^{-2}) for other months; for north China, the model consistently calculates smaller values throughout the year. On the other hand, the SUNYA CCM3, except during the April–June period, which has larger values (about 20–40 W m^{-2}), simulates quite well the pattern in the YHRV as well as in north China for other months. For LW CRF, both models produce stronger seasonal variations than the observations in both regions. For example, the January–June difference is about 40 W m^{-2} in the YHRV in the models, but the magnitude is only half of the value found in the observations.

b. Associations between cloud radiative forcing and cloud cover

As indicated above, model biases exist in the CRF, in particular in SW CRF over the YHRV in SUNYA

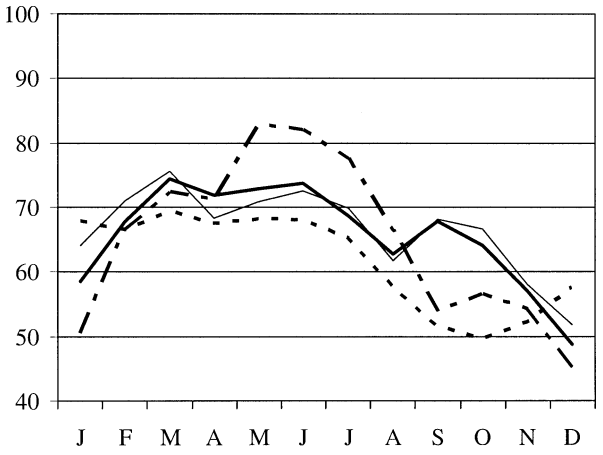

FIG. 4. The 1985–89 mean annual cycle of total cloud cover (%) over the YHRV from ISCCP (thick solid line), ground-based observation (thin solid line), SUNYA CCM3 (dashed–dotted line), and ECHAM4 (dashed line).

CCM3 data during the transition months from spring to summer and in the seasonal contrast in LW CRF. Since the SW CRF is closely correlated with the total cloud cover while the LW CRF correlates to high cloud, these biases in the CRF are expected to also be reflected in the biases in the model-simulated cloud cover.

Figure 4 shows the annual cycle of the total cloud cover over the YHRV for both the observations and the two model simulations. Note that there exists good agreement between the satellite and surface measurements (15-station mean values) in its seasonal variations, suggesting a mutual consistency in the two datasets. The observations illustrate an increasing cloud cover from January to March, then relatively large and constant values during April–June, followed by a decrease in July–August, then an increase to a second peak in September, and finally a decrease in the following months. The annual cycle reflects basically the movement of the rainbelt of the summer monsoon over the YHRV (Ding 1994).

However, the two models have quite different characteristics when compared with the observations. The ECHAM4 generally yields smaller values, with a maximum difference, ~15%, in September, which is consistent with the smaller SW CRF shown in Fig. 3b. On the other hand, the SUNYA CCM3 calculates a stronger annual cycle with much larger values in summer (May–July) and smaller values in other months, especially in the fall. The much larger simulated total cloud cover in summer contributes to the larger SW CRF shown in Fig. 3b. Note that the total cloud cover shows a small increase in October, which suggests a time lag (September in the observation; Fig. 3a) of 1 month for the southward withdrawal of the rainbelt, while the ECHAM4 does not exhibit such a feature.

We have also compared (not shown) the SUNYA CCM3 simulated and ISCCP high, middle, and low cloud cover. However, because of many factors (cloud overlapping treatment, the obscuring of middle- and low-level cloudiness by the high clouds in the ISCCP data, etc.), the differences are quite substantial. Therefore, instead of comparing the cloud cover at different levels, we examine the two associated parameters between the SW CRF and total cloud cover, and the LW CRF and high cloud cover. In addition, from Fig. 3, there are two biases in the simulation. First, in the YHRV, the larger annual amplitude is caused mainly by the significantly larger value in May. Second, in north China the maximum of the SW CRF occurs in May rather than in July, as in the observations. On the other hand, the simulations in south China agree well with the observations (not shown), in both the amplitude and the phase. Therefore, we focus on analyzing the May simulations.

Figure 5 shows a scatter diagram of the SW CRF versus total cloud cover. Note that the observations have a resolution of $2.5° \times 2.5°$ while SUNYA CCM3 uses T42 resolution of $2.8° \times 2.8°$. The model shows distinctive differences from the observations in two major patterns. First, the model shows a larger spread in the ranges; for example, for north China, the majority of the total cloud cover is within 20%–95% while the observations are much narrower, within 40%–80%. Second, different regions exhibit different characteristics in the associations between SW CRF and cloud cover. The observed linear relationship is maintained in the model simulations in north China (nearly the same slope) and the YHRV (steeper slope), but it is less clear in south China. In addition, the model has the tendency to simulate a stronger effect of clouds on the SW CRF, which, as discussed below, is caused by larger simulated middle cloud cover. Figure 6 shows a scatter diagram of LW CRF versus high cloud cover. Although the mean LW CRF is comparable between the observations and model simulations, the cloud cover discrepancy is quite substantial in both the mean and the spreads.

c. Analysis of SUNYA CCM3 model bias

In this section, we use the temperature and moisture data simulated from the SUNYA CCM3 to provide some insights into the SW and LW CRF biases. In particular, we focus on May, since as shown in Fig. 3, the SW CRF bias in the annual cycle of the SUNYA CCM3 over the YHRV is mainly due to the much larger value in this month. There are two primary parameters, the cloud water and cloud cover, that affect the SW CRF. In May, the model has a dry bias (see Fig. 7) when compared with the National Centers for Environmental Prediction–National Center for Atmospheric Research (NCEP–NCAR) reanalysis data. Since an empirical relationship between cloud water and the column water vapor is used in the model (Kiehl et al. 1996), the smaller water vapor also implies smaller cloud water. The results are also consistent with Hack et al. (1998), who

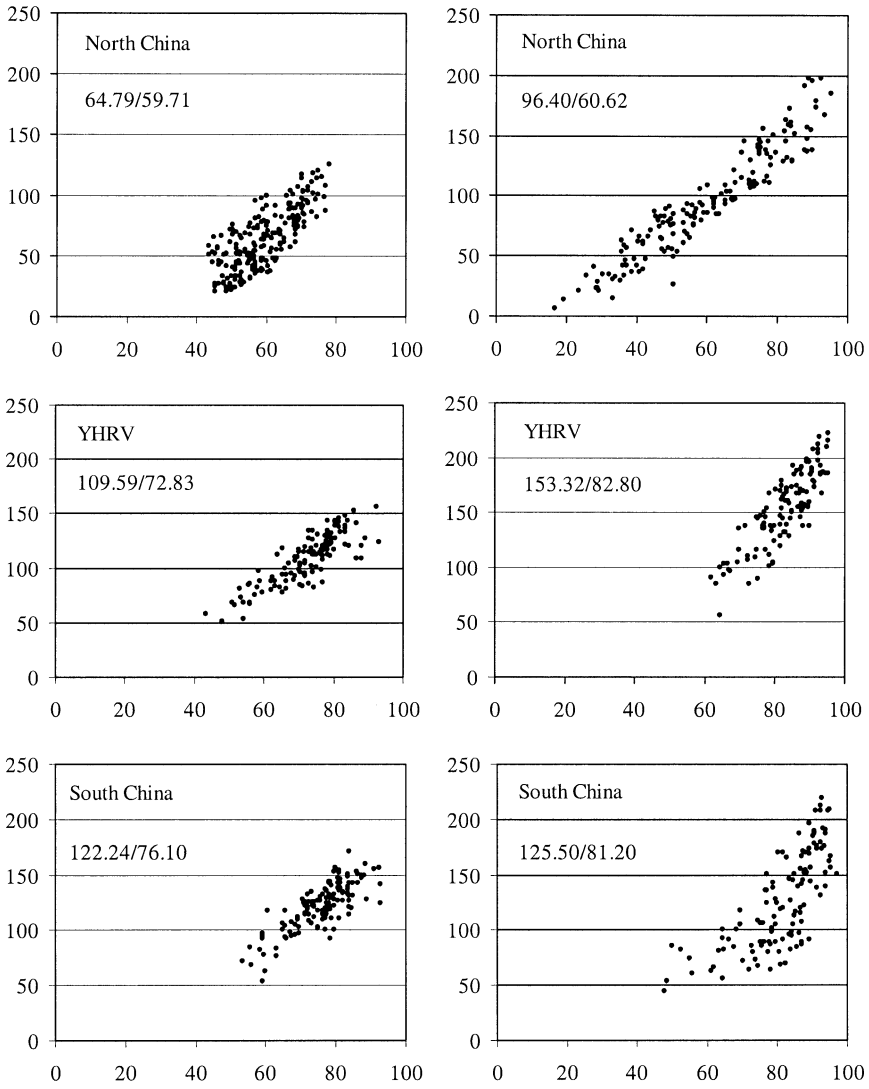

FIG. 5. Shortwave CRF (W m^{-2}; *y* axis) vs total cloud cover (*C*; %) for (left) observations and (right) SUNYA CCM3 simulations. Mean values of CRF/*C* over the ensembles are given.

showed that in summer (June–July–August; JJA) the CCM3 simulates less (about 20%) column water vapor in East Asia as well as smaller (by 30%–100%) zonal mean cloud liquid water paths for 23°–43°N. Nevertheless, these results indicate that the smaller amount of cloud water, which can yield an even smaller SW CRF, is not the cause for the model bias in SW CRF.

On the other hand, the bias in the vertical distribution of cloud cover can contribute to the bias in the SW CRF. This point can be illustrated through the comparison between model biases in the May monthly mean values over the YHRV and south China. In Table 1, we list the observed and SUNYA CCM3 simulated high, middle, low, and total cloud cover amounts as well as the associated LW and SW CRFs for these two regions. The comparison between the observations and the model indicates significant differences over the YHRV, but excellent agreement in south China. The contrast, which to some extent can be attributed to a larger difference in total cloud cover over the YHRV than that over south China, is more importantly caused by the much smaller middle-level clouds simulated in south China. For example, over the YHRV, the middle clouds are 40% in the model compared with 26% from the observations, while over south China they are 17% in the model compared with 27% from the observations. (Note however that the observations also have a significant bias especially for low cloud cover.) Thus, over south China the smaller middle-level clouds compensate for the effect of larger low-level clouds, and lead to much better agreements in the SW CRF with the observations. On the other hand, the stronger effect of cloud cover on the SW CRF in the YHRV is caused by a larger simulated middle cloud cover.

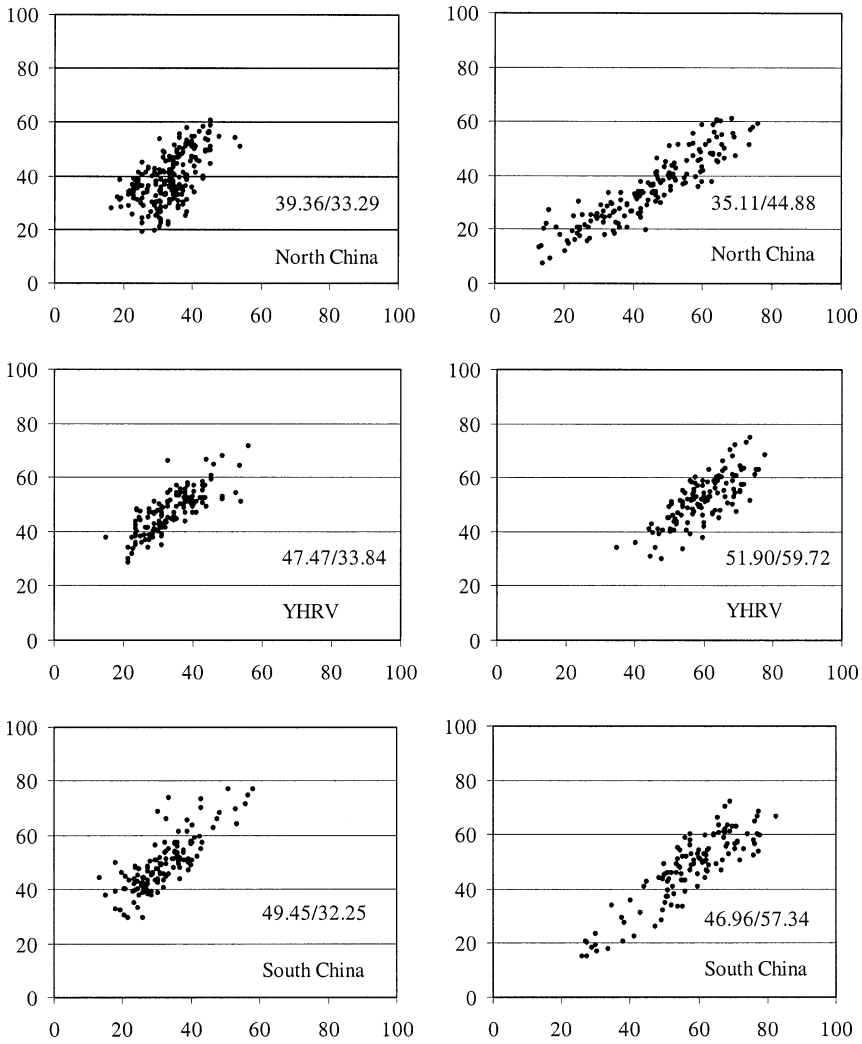

FIG. 6. Same as in Fig. 5 except for longwave CRF vs high cloud cover.

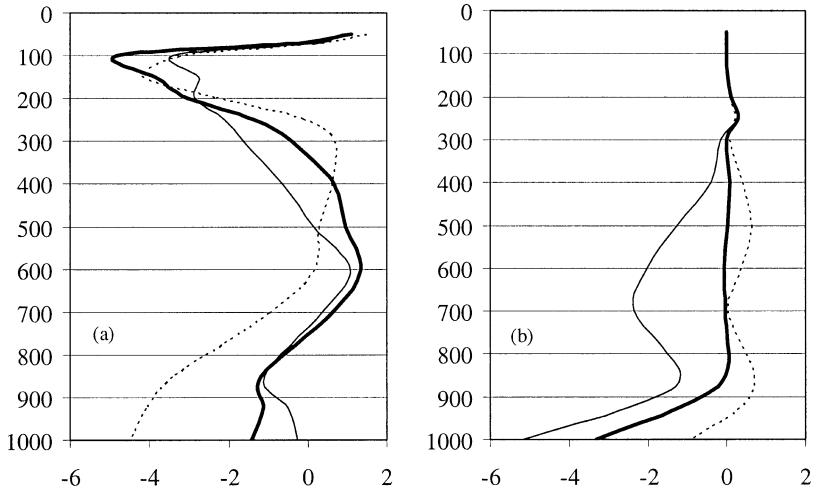

FIG. 7. May monthly mean vertical distributions of SUNYA CCM3 biases (from the NCEP–NCAR reanalysis) in (a) temperature (°C) and (b) moisture (g cm^{-3}) of north China (thin dashed line), the YHRV (thick solid line), and south China (thin solid line).

TABLE 1. May monthly mean observed and model-simulated high, middle, low, and total cloudiness (%), and the SW and LW CRF (W m^{-2}) for the YHRV (30°–34°N, 105°–122°E). Note that the monthly mean high, middle, and low cloud cover amounts are calculated based on the cloud cover at each time step, taking into consideration the vertical cloud overlapping.

	YHRV		South China	
Parameter	Observations	SUNYA CCM3	Observations	SUNYA CCM3
High	33.84	59.72	32.25	57.34
Middle	26.67	40.37	27.14	17.79
Low	14.58	54.78	19.15	54.78
Total		82.80		81.20
ISCCP	72.83		76.10	
Ground-based data	70.87		78.62	
SW CRF	−109.59	−153.32	−122.24	−125.50
LW CRF	47.47	51.90	27.39	21.16

Next, we diagnosed the bias in LW CRF. As shown in section 3a, the SUNYA CCM3 simulates smaller LW CRF, except in May and June in the YHRV; for example, in April, the simulated value is 38 W m^{-2} (versus an observed value of 53 W m^{-2}) over the YHRV. On the other hand, the high cloud is much larger in the simulation, especially in April–August; for example, the high cloud values are larger with ranges from 15% to 30% in these months. Therefore, it appears that the bias in smaller values of LW CRF is not consistent with larger values of high clouds because of their positive correlation indicated earlier. To investigate this inconsistency, we analyze the temperature profile because the LW CRF depends not only on the high cloud cover but also on the temperature difference between the surface and the cloud level.

As an example, Fig. 7 shows the vertical profile of the temperature bias against the NCEP–NCAR reanalysis in May in the YHRV and over north China. Note that the tropopause is at 100 hPa for the simulation. It can be seen that the SUNYA CCM3 simulates a too cold planetary boundary layer (above 750 hPa) as well as the regions below 200 hPa. The cold bias in the troposphere is also verified using the station observations. On the other hand, the model simulates a small and mostly positive bias between 200 and 750 hPa. We observe that the difference in the temperature bias at the upper troposphere and the surface is not large, and this difference will not contribute to the smaller simulated LW CRF. This implies that the simulated high cloud resides at a lower altitude (below 200 hPa), where the model simulates warmer climate, and therefore the high cloud longwave radiation emission is enhanced. In contrast, the clear-sky surface emission is reduced due to the colder surface temperature. It is this contrast that contributes to the smaller LW CRF, when there is more high cloud cover.

4. Remarks

It is quite clear that cloud radiative forcing over east China shows distinctive latitudinal and seasonal characteristics, in particular in the transition from late spring to summer over south China and the Yangtze-Huai River valley. Although these transitions are consistent with changes in total cloud cover, the effects of the changes in the cloud vertical distribution may also play an important role and needs further clarification.

In addition, there are two aspects associated with cloud radiative forcing that warrant further study. First, given the large magnitude of CRFs in the transitional months, it will be important to compare those values with other heating/cooling sources (e.g., latent heating) and evaluate their role in affecting large-scale circulation. Second, since the cloud radiative forcing is a bulk variable involving several cloud parameters (cover, microphysics, liquid/ice water, and the radiation fluxes), it would be ideal to use it for evaluating and comparing the climate simulations from the AMIP-II and Coupled Model Intercomparison Project-II (CMIP-II) models without considering the different parameterizations of the cloud parameters adopted in the models.

Acknowledgments. This is a collaborative research study performed under the auspice of AMIP-II and CMIP-II Subproject 25 (General Circulation Model Simulation of the East Asian Climate). The work at SUNYA was supported by the Office of Basic Energy Science (BES) U.S. Department of Energy Grant DE-FG02-92ER61369.

REFERENCES

Barkstrom, B. R., 1984: The Earth Radiation Budget Experiment (ERBE). *Bull. Amer. Meteor. Soc.,* **65,** 1170–1185.

Cess, R. D., M. Zhang, B. A. Wielicki, D. F. Young, X. Zhou, and Y. Nikitenko, 2001: The influence of the 1998 El Niño upon cloud-radiative forcing over the Pacific warm pool. *J. Climate,* **14,** 2129–2137.

Ding, Y.-H., 1994: *Monsoons over China.* Kluwer Academic, 419 pp.

Fu, R., A. D. Del Genio, and W. B. Rossow, 1990: Behavior of deep convective clouds in the tropical Pacific deduced from ISCCP radiances. *J. Climate*, **3,** 1129–1152.

Gates, W. L., and Coauthors, 1999: An overview of the results of the Atmospheric Model Intercomparison Project (AMIP I). *Bull. Amer. Meteor. Soc.,* **80,** 29–56.

Hack, J. J., J. T. Kiehl, and J. W. Hurrell, 1998: The hydrologic and

thermodynamic characteristics of the NCAR CCM3. *J. Climate*, **11,** 1179–1206.

Harrison, E. F., B. R. Barkstrom, V. Ramanathan, R. Cess, and G. Gibson, 1990: Seasonal variation of cloud radiative forcing derived from the Earth Radiation Budget Experiments. *J. Geophys. Res.*, **95,** 18 687–18 703.

Kiehl, J. T., and V. Ramanathan, 1990: Comparison of cloud forcing derived from the Earth Radiation Budget Experiment with that simulated by the NCAR Community Climate Model. *J. Geophys. Res.*, **95,** 11 679–11 698.

——, J. J. Hack, G. B. Bonan, B. A. Boville, B. P. Briegleb, D. L. Williamson, and P. J. Rasch, 1996: Description of the NCAR Community Climate Model (CCM3). NCAR Tech. Note NCAR/TN-420+STR, Boulder, CO, 152 pp.

Liang, X.-Z., and W.-C. Wang, 1997: Cloud overlap effects on general circulation model climate simulations. *J. Geophys. Res.*, **102,** 11 039–11 047.

——, ——, and A. N. Samel, 2001: Biases in AMIP model simulations of the east China monsoon system. *Climate Dyn.*, **17,** 291–304.

Minnis, P., P. W. Heck, and D. F. Young, 1993: Inference of cirrus cloud properties using satellite-observed visible and infrared radiances. Part II: Verification of theoretical cirrus radiative properties. *J. Atmos. Sci.*, **50,** 1305–1322.

Ockert-Bell, M. E., and D. L. Hartmann, 1992: The effect of cloud type on Earth's energy balance: Results for selected regions. *J. Climate*, **5,** 1157–1171.

Potter, G. L., J. M. Slingo, J.-J. Morcrette, and L. Corsetti, 1993: A modeling perspective on cloud radiative forcing. PCMDI Rep. 9, 23 pp.

Randall, D. A., Harshvardhan, D. A. Dazlich, and T. G. Corsetti, 1989: Interactions among radiation, convection, and large-scale dynamics in a general circulation model. *J. Atmos. Sci.*, **46,** 1943–1970.

Rossow, W. B., and R. A. Schiffer, 1991: ISCCP cloud data products. *Bull. Amer. Meteor. Soc.*, **72,** 2–20.

Samel, A. N., W.-C. Wang, and X.-Z. Liang, 1999: The monsoon rainband over China and relationships with the Euroasian circulation. *J. Climate*, **12,** 115–131.

Wang, W.-C., W. Gong, and H. Wei, 2000: A regional model simulation of the 1991 severe precipitation event over the Yangtze–Huai River valley. Part I: Precipitation and circulation statistics. *J. Climate*, **13,** 74–92.

Weare, B. C., 1995: Factors controlling ERBE longwave clear-sky and cloud forcing fluxes. *J. Climate*, **8,** 1889–1899.

Wong, S., and W.-C. Wang, 2000: Inter-hemispheric asymmetry in the seasonal variation of the zonal mean tropopause. *J. Geophys. Res.*, **105,** 26 645–26 659.

Zhang, M. H., R. D. Cess, and S. C. Xie, 1996: Relationship between cloud radiative forcing and sea surface temperatures over the entire tropical oceans. *J. Climate*, **9,** 1374–1384.